Improving tropospheric corrections on large-scale Sentinel-1 interferograms using a machine learning approach for integration with GNSS-derived zenith total delay (ZTD)

Roghayeh Shamshiri[a],[*], Mahdi Motagh[b],[c], Hossein Nahavandchi[a], Mahmud Haghshenas Haghighi[b],[c], Mostafa Hoseini[a]

[a] Department of Civil and Environmental Engineering, Norwegian University of Science and Technology (NTNU), Trondheim 7491, Norway
[b] GFZ German Research Centre for Geosciences, Department of Geodesy, Section of Remote Sensing and Geoinformatics, Potsdam 14473, Germany
[c] Institute for Photogrammetry and GeoInformation, Leibniz University Hannover, Hannover 30167, Germany

ABSTRACT

Sentinel-1 mission with its wide spatial coverage (250 km), short revisit time (6 days), and rapid data dissemination opened new perspectives for large-scale interferometric synthetic aperture radar (InSAR) analysis. However, the spatiotemporal changes in troposphere limits the accuracy of InSAR measurements for operational deformation monitoring at a wide scale. Due to the coarse node spacing of the tropospheric models, like ERA-Interim and other external data like Global Navigation Satellite System (GNSS), the interpolation techniques are not able to well replicate the localized and turbulent tropospheric effects. In this study, we propose a new technique based on machine learning (ML) Gaussian processes (GP) regression approach using the combination of small-baseline interferograms and GNSS derived zenith total delay (ZTD) values to mitigate phase delay caused by troposphere in interferometric observations. By applying the ML technique over 12 Sentinel-1 images acquired between May–October 2016 along a track over Norway, the root mean square error (RMSE) reduces on average by 83% compared to 50% reduction obtained by using ERA-Interim model.

1. Introduction

The fast, accurate, and cost-effective detection and mapping of ground instabilities at regional to national scales can be extremely helpful for civil protection authorities. Such maps can be used for planning effective proactive measures and implementing warning systems for the areas prone to risk (Emadali et al., 2017; Milillo et al., 2018). Even if ground deformation cannot be prevented or stopped, it must be accounted for in new construction planning.

Classical geodetic methods such as observations made by permanent global navigation satellite system (GNSS) stations allow monitoring of ground deformation at high temporal resolution with millimeter-level accuracy. However, they can provide the information only at discrete and predefined spatial locations, rather than spatially continuous deformation field. By contrast, surface deformation maps provided by space technology via Interferometric Synthetic Aperture Radar (InSAR) have an expanded spatial and temporal coverage. InSAR is capable of capturing the full continuous deformation field with a spatial-resolution on the order of 1–20 m and temporal-resolution of 6–45 days over

hundreds of square kilometers. The potential of InSAR for mapping large-scale deformation (Cetin et al., 2014; Daout et al., 2017; Hussain et al., 2018; Kaneko et al., 2013; Motagh et al., 2010) has further been facilitated and improved thanks to Sentinel-1 mission, operated by the European space agency (ESA) (Haghshenas Haghighi and Motagh, 2018; Kalia et al., 2017; Raspini et al., 2018). The interferometric wide swath (IW) acquisition mode can image a 250-km swath, which makes it possible to routinely generate large-scale interferograms by seamlessly concatenating consecutive frames of data along the acquisition track (Ferretti et al., 2015; Torres et al., 2012). However, despite the potential to generate large-scale interferograms, the spatiotemporal variability of the troposphere, limits InSAR measurements accuracy (Delacourt et al., 1998; Haghshenas Haghighi and Motagh, 2017). For instance, 20% change in relative humidity leads to 10 cm error in the final deformation map (Zebker et al., 1997). Tropospheric phase delays may be mitigated by applying the time filtering implemented in advanced multi-temporal InSAR (MTI) methods. These techniques are typically applied on the original interferograms and have been widely used to measure the Earth's surface deformations related to subsidence/

uplift (Haghshenas Haghighi and Motagh, 2019; Lubitz et al., 2013; Motagh et al., 2017; Shamshiri et al., 2014), landslide (Haghshenas Haghighi and Motagh, 2016; Intrieri et al., 2018; Mirzaee et al., 2017), tectonic (Feng et al., 2017; Fielding et al., 2017; Motagh et al., 2010), and volcanoes (Morales Rivera et al., 2017; Spaans and Hooper, 2016; Walter and Motagh, 2014). The MTI techniques can be broadly classified into three main categories, which are (1) persistent scatterer (PS) (Ferretti et al., 2001; Hooper et al., 2004), (2) small baseline (SBAS) approach (Berardino et al., 2002), and (3) hybrid methods, such as SqueeSAR™ (Ferretti et al., 2011; Raspini et al., 2013; Shamshiri et al., 2018; Solari et al., 2018). Studies have shown that applying MTI methods on the tropospherically corrected interferograms further improves the accuracy of the final results (Jo et al., 2010; Samsonov et al., 2014; Tang et al., 2018; Vajedian et al., 2015).

One way to correct for tropospheric delays in interferograms is using external sources such as the meteorological models like ERA-Interim/ERA5 (Hu and Mallorquí, 2019; Jolivet et al., 2011). ERA-Interim is a global atmospheric reanalysis calculated by the European center for medium-range weather forecast (ECMWF). The system provides several meteorological variables, including pressure, temperature, and relative humidity at 6-hour intervals, and horizontal resolution of approximately 79 km, with 60 levels in vertical (Berrisford et al., 2011). The data are temporally and spatially interpolated to find the tropospheric phase delay at SAR observation system. However, the horizontal resolution of the ERA-Interim is not fine enough to capture the small scale turbulent mixing effect in InSAR observations.

One alternative is to use GNSS-based techniques (Onn and Zebker, 2006; Williams et al., 1998; Yu et al., 2018). The zenith total delay (ZTD) can be accurately derived at the highest temporal resolution (15–30 min (Herring et al., 2018)) among the available external datasets, from each GNSS receiver. Using densely distributed GNSS stations we can map phase delay into SAR line-of-sight (LOS) direction. However, the ZTDs derived at the GNSS receivers should be interpolated at the SAR pixel size, which is a challenging task, especially in areas with rugged topography and large meteorological contrasts. Using interpolation methods leads to distorted extrapolation/interpolation in areas exceeding the maximum altitude of the GNSS stations and in areas with steep topography. Moreover, it is expected that these methods are limited to map the effect of turbulent mixing.

To overcome these problems, we implement a new method for tropospheric correction of large-scale Sentinel-1 interferograms based on a machine learning (ML) approach, which exploits short-interval interferograms and ZTD values at GNSS stations. ML approaches have been widely used and demonstrated their predictive accuracy in fields of data mining (Bellinger et al., 2017), pattern recognition (Viola and Jones, 2001), regression (Huang et al., 2012), classification (Liaw et al., 2002), and spatial interpolation (Li et al., 2011). They are also successfully employed in remote sensing applications (Zhu et al., 2017) such as classification of hyper-spectral images (Chen et al., 2015; Santara et al., 2017), interpretation of SAR and high-resolution satellite images (Chen et al., 2016; Duan et al., 2017; Hu et al., 2015; Zhao et al., 2016a), data fusion (Huang et al., 2015; Zhong et al., 2016), 3-D reconstruction (Blaha et al., 2016; Hane et al., 2013), and interferometric phase unwrapping (Sawaf and Groves, 2014; Spoorthi et al., 2019). We focus on Norway, and use the unwrapped differential phase derived by large-scale interferograms of Sentinel-1 with short temporal baselines as primary input variables and the GNSS stations location as secondary input variables for the model training. We use the differential ZTDs (dZTD) derived at the GNSS stations at two acquisition times as the response variables. We then use the model to predict the corresponding dZTD values for the whole interferogram. The estimated dZTD maps can be used to compute the dZTD maps for the interferograms with larger temporal baselines before applying the SBAS analysis. We show that applying this approach on interferograms further improves the quality of InSAR time-series analysis in comparison to those cases, where interferograms are corrected by ERA-Interim.
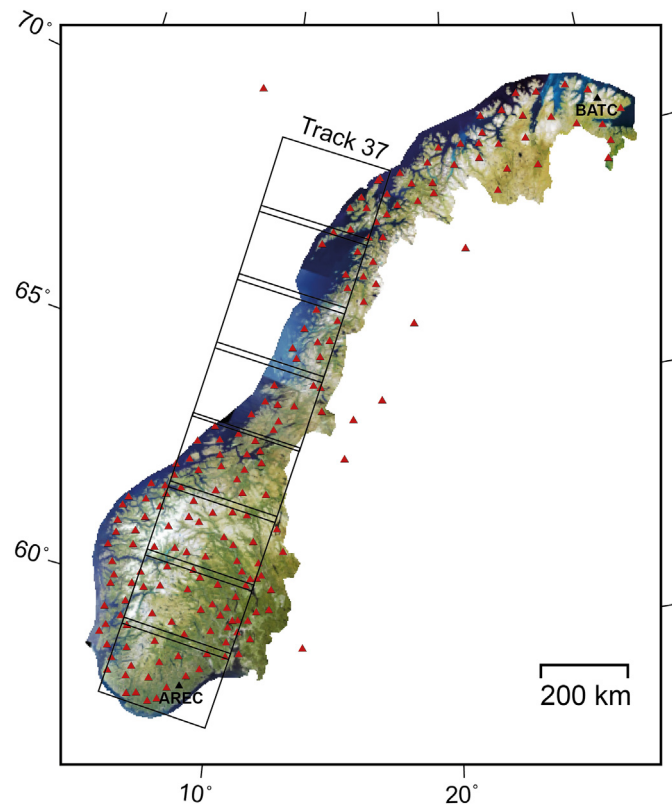

Fig. 1. The outlines of the Sentinel-1 frames along the track number 37 represented by the rectangles, superimposed on the aerial image (norgeskart.no). Red triangles show the permanent Norwegian mapping authority (NMA) GNSS stations in mainland Norway, IGS, and EUREF GNSS stations. (For interpretation of the references to color in this figure legend, the reader is referred to the web version of this article.)

In the following sections we first present the dataset employed for this study, then describe the methodology and the applied ML techniques. Then we evaluate the tropospheric corrections results using different methods and finally discuss the results in terms of the performance of the applied techniques.

2. Data processing

2.1. Interferometric processing

We use 12 SLC images of Sentinel-1 acquired in IW mode covering May–October 2016 from descending track number 37. The outline of the frames is shown in Fig. 1.

We build the interferograms using the GAMMA software (Wegmüller and Werner, 1997). We first concatenate consecutive frames of the images along the acquisition track, and select one concatenated scene as a master (29 July 2016) to provide the reference geometry. The remaining concatenated images are co-registered and re-sampled to the master reference geometry using terrain height and precise orbit geometry, followed by intensity matching and spectral diversity refinement methods (Fattahi et al., 2016; Nannini et al., 2016; Prats-Iraola et al., 2012; Scheiber and Moreira, 2000) for coregistration. Subsequently, an optimal small baseline network of interferograms is defined by considering a maximum temporal baseline of 36 days. Fig. 2 shows the network.

The multi-looked interferograms have been generated with 10 and 2 looks in the range and the azimuth direction, respectively. Initial topographic phase components are subtracted from the small-baseline interferograms using a re-sampled digital elevation model (DEM) at 90-m pixel spacing provided by the Norwegian Mapping Authority (NMA).
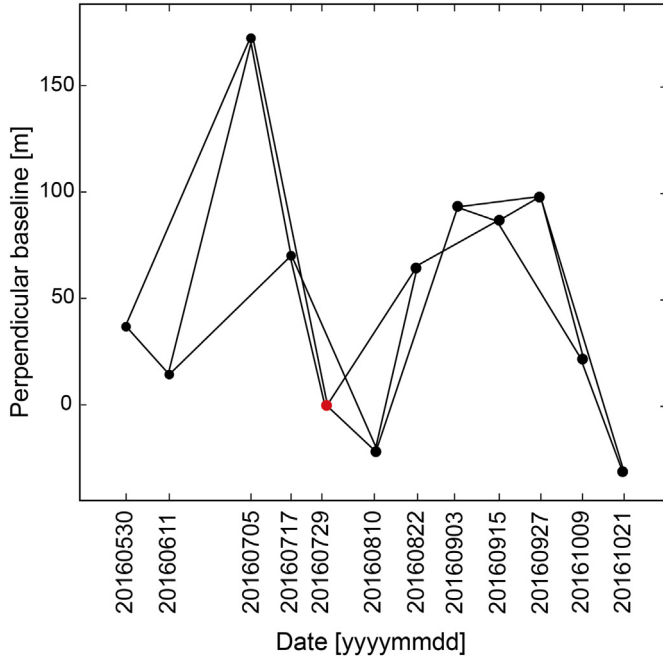
Fig. 2. Plot of the acquisition dates versus the perpendicular baselines for the network of the Sentinel-1 data. The black circles represent the slave images and the red one shows the master image. The lines represent the small-baseline interferograms. (For interpretation of the references to color in this figure legend, the reader is referred to the web version of this article.)

The interferograms are geocoded using the same DEM. Finally, two-dimensional phase unwrapping is performed on the small-baseline interferograms for pixels with a coherence greater than 0.2.

2.2. ERA-Interim

As mentioned earlier, ERA-Interim provides among other meteorological variables, pressure (P), temperature (T), and relative humidity (e). Putting these meteorological data in Eq. (1), the $ZTD^{(i)}$ at a specific height $h^{(i)}$ can be derived by integrating the hydrostatic and wet components from height h to the top of the troposphere, h^{top} (considered 30 km in this study) (Doin et al., 2009; Hanssen, 2001).

$$ZTD^{(i)} = 10^{-6} \int_{h^{(i)}}^{h^{top}} ((K_1\frac{P}{T})_{hydro} + (K_2'\frac{e}{T} + K_3\frac{e}{T^2})_{wet})dh, \qquad (1)$$

where $K_1 = 77.6$ KhPa^{-1}, $K_2' = 23.3$ KhPa^{-1}, and $K_3 = 3.75 \times 10^5$ K^{2}hPa^{-1} (Smith and Weintraub, 1953).

We use the TRAIN toolbox, which performs a linear interpolation in time, and a lateral and vertical spline interpolation of P, T, and e, then computes the ZTD for each node at the SAR acquisition time using Eq. (1) (Bekaert et al., 2015). Afterwards, we map them into the Sentinel-1 LOS direction, using Eq. (2):

$$STD = \frac{ZTD}{\cos\theta_i}, \qquad (2)$$

where θ_i is the incidence angle of the radar signal for the resolution cell i, and STD is the slant total delay (STD). Finally, using Eq. (3), we can convert the STD map from pseudo-range to phase delay, ϕ_{trop}.

$$\phi_{trop} = -\frac{4\pi}{\lambda}STD, \qquad (3)$$

where λ is the Sentinel-1 wavelength.

2.3. GNSS processing

In order to calculate the tropospheric phase delay, we exploit roughly 200 permanent GNSS stations (CPOS) provided by the Norwegian mapping authority (NMA), with the separation between adjacent stations ranging from 13 km to 70 km, and around 50–60 km on average (Jacobsen and Schäfer, 2012). We also use four international GNSS service (IGS), and five EUREF permanent network (EPN) stations. Fig. 1 shows the location of the GNSS stations.

To derive the ZTD values from the GNSS receivers, we use the GAMIT software package (Herring et al., 2018). For this, we first divide the GNSS data into six clusters, and add the observations from the EPN and IGS sites into all of the cluster solutions to constrain the network solutions. Then we process each sub-network separately for each acquisition day of SAR data at 2-hour intervals using the network-based solution in GAMIT software package. Afterwards, we map them into the Sentinel-1 LOS to derive STD using Eq. (2).

The STDs derived at the GNSS receivers should be interpolated at the SAR pixel size, which is a challenging task. Because of the rugged topography and the large meteorological contrasts throughout Norway, the spatiotemporal variability in the ZTD is high. Considering the GNSS data used in this study, the variability ranges from ∼ 32 cm to ∼ 45 cm in space, and reaches to ∼ 18 cm during a day. Fig. 3a shows the ZTD
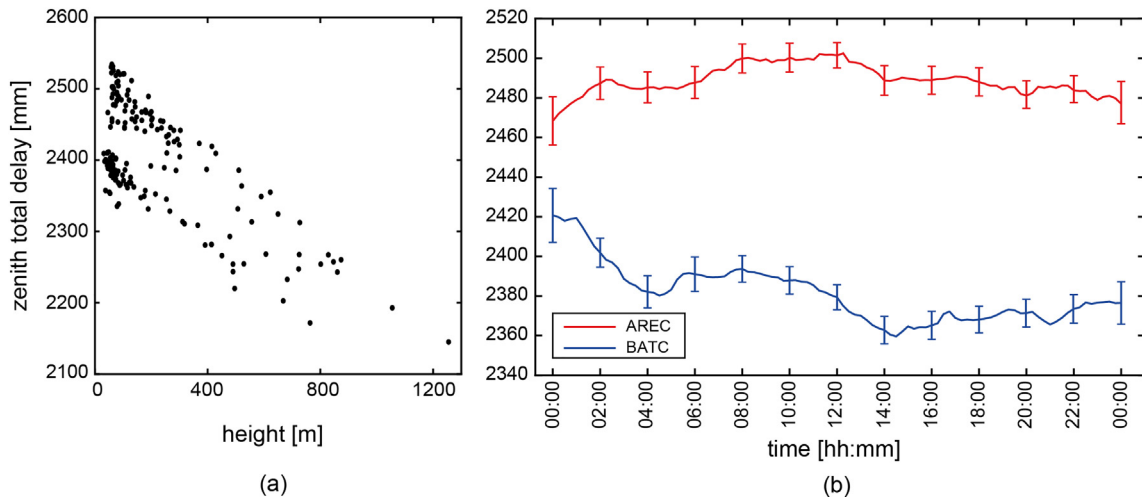

Fig. 3. (a) The zenith total delay versus elevation at each GNSS stations in September 15th, 2016, (b) the ZTD values in time at two GNSS stations, AREC and BATC, located at the same elevation (see Fig. 1 for their location). The bars show the standard deviations at each hour.

values versus the elevation at each GNSS stations in Norway on September 15th, 2016. It can be seen that although there is a inverse correlation between the ZTD and the elevation, the ZTDs differ between two stations located at the same elevation. As an example, we plot in Fig. 3b the changes in ZTD values over time at two GNSS stations, called AREC and BATC, located in southern and northern Norway (black colored triangles in Fig. 1). Even though they are at the same elevation (~78.8 m), their ZTD show totally different behavior in time. This makes it necessary to accurately estimate the tropospheric artifacts and remove them from the interferograms. It also shows that one single ZTD-elevation relationship is not applicable for a scene the size of Norway.

In order to interpolate the delay due to tropospheric stratification, which correlates with topography, different approaches have been suggested including spatial structure function (Li et al., 2006), iterative tropospheric decomposition (ITD) (Yu et al., 2017), seasonal Gaussian function (Hu and Yao, 2018), and least-squares collocation (Wilgan and Geiger, 2018). However, as mentioned above, the ZTD-elevation distribution in Norway for different dates, shows complex patterns and vary in time, which makes it difficult to fit a specific function to the data. In the following section, we explain how we can exploit machine-learning for such data integration between GNSS and interferometric observations for tropospheric correction.

2.4. Machine learning approach

We propose a new method based on ML approach using combination of GNSS and small baseline (SB) interferograms with short temporal baselines to model and correct tropospheric effects in interferometric phase. Fig. 4 shows the flowchart of our algorithm. We first select interferograms with small temporal baselines (12 days in this study). For each of these interferograms, we train a model using the available GNSS stations, by this assumption that the ground surface displacement is negligible at the permanent GNSS stations, and the interferograms are mainly affected by the tropospheric phase delays. The differential unwrapped phases at the location of the GNSS stations are used as primary variables, and the location of the stations (ϕ, λ) are used as the secondary variables for the inputs of the training. We then exploit differential STDs at GNSS stations as the response of the model.

After preparing the training datasets (the inputs and the responses) for interferograms with small temporal baselines we apply on our datasets several ML-based approaches including linear regression, support vector machine (SVM) (Cortes and Vapnik, 1995), as well as Gaussian processes (GP) regression (Rasmussen, 2004). The modeling is performed by minimizing an objective function, which is the root-mean-square error (RMSE) in this study. We use a 5-fold cross-validation to validate the trained model. For this, we randomly partition our dataset into five disjoint sub-datasets. Four sub-datasets are combined and used for the model training and the held-out one, the so-called validation dataset, is used to check the prediction of the trained model. This

process is repeated by varying the validation dataset until all five sub-datasets are used for validation. The performance of the models is then assessed by the average RMSE on all datasets, when they are kept in a held-out fold. Consequently, all methods are applied to the same training and test datasets, and the model corresponding to the lowest RMSE is selected. In the next step, the selected model, which is able to predict the STD at each GPS stations in the interferogram, is used to predict the differential STD values at all pixels in the interferogram. This procedure of training is re-performed for each interferogram with small temporal baseline in the network (Fig. 2).

During model training, it may happen that the training error becomes very small, but prediction error for the new data becomes large. This is a well-known problem in machine-learning referred to as overfitting (Dietterich, 1995; Domingos, 2012). To avoid this, we add the elevation of the stations in those interferograms suffering from overfitting as the secondary variables. It is worth noting that phase unwrapping errors in the islands relative to the mainland due to the water separation are visually identified and manually removed from all the interferograms before the ML-running. Therefore, the GNSS stations, which are located in the areas affected by the unwrapping errors, are considered as outliers in the model training and are discarded from the modeling.

In our experience, among the mentioned methods, GP leads to the most accurate prediction (the RMSE of the training is up to around 2.5 radians; 10 mm), as it has been also concluded in other studies (Bélisle et al., 2015). We apply GP with different covariance functions for each dataset and select the one with the lowest RMSE.

GP regression is a non-parametric, supervised learning method. Let $S = \{x^{(i)}, y^{(i)}\}_{i=1}^{n}$ be a set of training points where, $x^{(i)}$ is the differential phases at the GNSS stations and the GNSS locations as the inputs, and $y^{(i)}$ is the differential STD at the GNSS stations as the response. The objective is to learn a function f projecting the input vector x into a target function y, as

$$y^{(i)} = f(x^{(i)}) + \epsilon^{(i)}, \quad i = 1, ..., n \tag{4}$$

where, ϵ is noise variable with $\mathcal{N}(0, \sigma_n^2)$ distribution, and f is assumed to be a zero-mean Gaussian process prior with covariance function $k(.,.)$,

$$f(.) \sim \mathcal{GP}(0, k(.,.)) \tag{5}$$

Now, let $T = \{x_*^{(i)}, y_*^{(i)}\}_{i=1}^{n_*}$ as a set of testing points, which must have a Gaussian distribution similar to the training data:

$$\begin{bmatrix} \vec{y} \\ \vec{y_*} \end{bmatrix} \Big| x, x_* = \begin{bmatrix} \vec{f} \\ \vec{f_*} \end{bmatrix} + \begin{bmatrix} \vec{\epsilon} \\ \vec{\epsilon_*} \end{bmatrix} \sim \mathcal{N} \left(\vec{0}, \begin{bmatrix} k(x, x) + \sigma_n^2 I & k(x, x_*) \\ k(x_*, x) & k(x_*, x_*) + \sigma_n^2 I \end{bmatrix} \right) \tag{6}$$

Using the rules for conditioning Gaussian, we will have (Do, 2007):

$$\vec{y_*} | \vec{y}, x, x_* \sim \mathcal{N}(\mu^*, \Sigma_n^*) \tag{7}$$
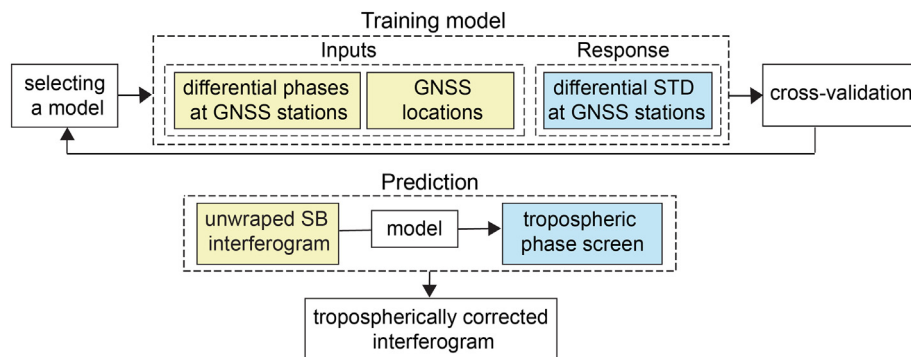
where,

Fig. 4. Flow diagram of the implemented tropospheric correction method from the small temporal baseline interferogram in this study.
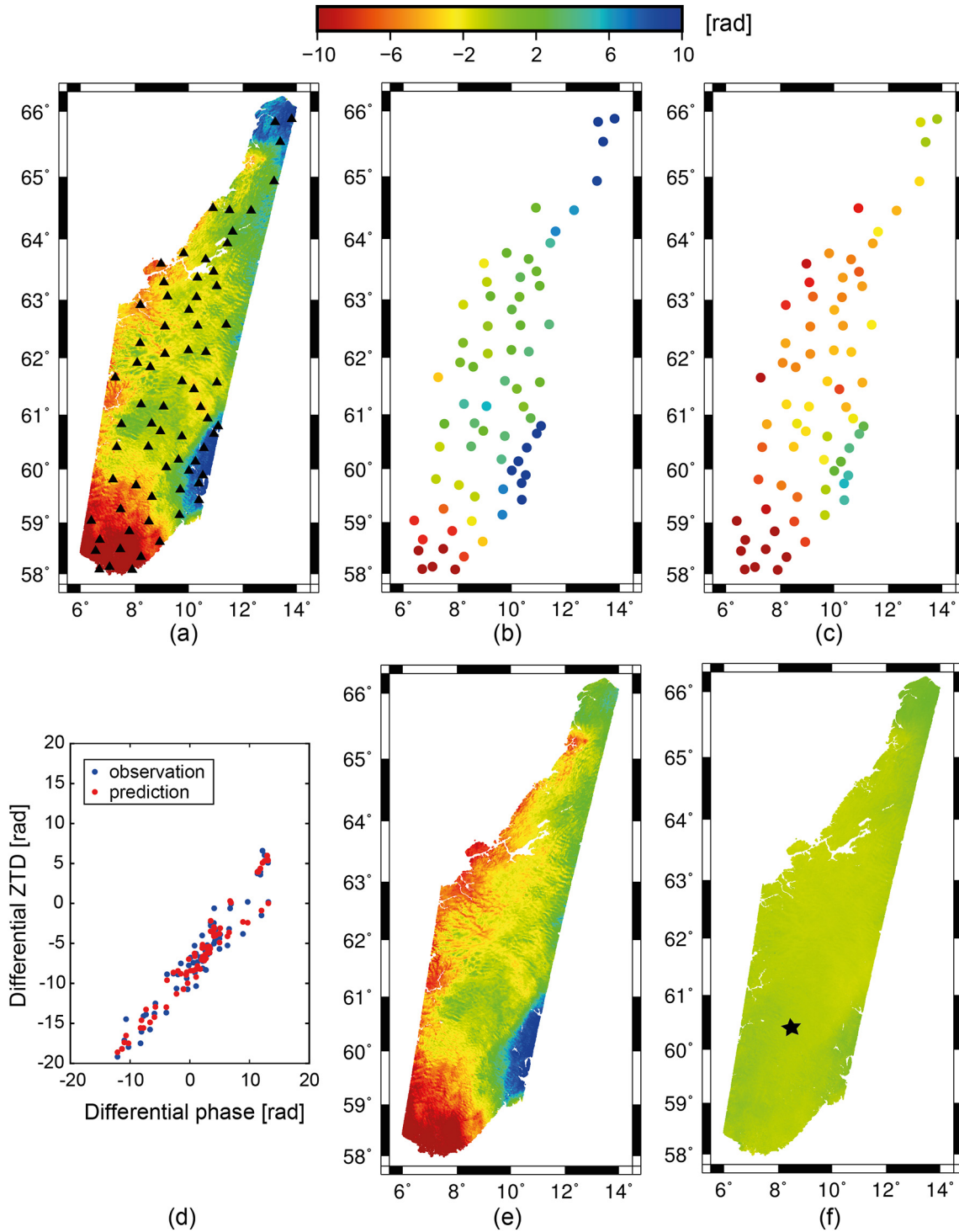
Fig. 5. An example of tropospheric corrections from InSAR and GNSS-based method (using machine learning) on the interferogram "20160927–20161009", where date is in yyyymmdd-yyyymmdd format. (a) shows the original interferogram, (b–c) the unwrapped phases of the original interferograms and the differential STD values at the GNSS locations, respectively. (d) shows the training of the model, (e) the predicted differential STD, and (f) the corrected interferogram. The triangles in (a) show the location of the GNSS stations. The star in (f) shows the location of the reference area, which is one of the GNSS stations, and set for the all interferograms and STD maps.

$$\mu^* = k(x_*, x)(k(x, x) + \sigma_n^2 I)^{-1}\vec{y}$$
$$\Sigma_n^* = k(x_*, x_*) + \sigma_n^2 I - k(x_*, x)(k(x, x) + \sigma_n^2 I)^{-1}k(x, x_*) \tag{8}$$

are the estimate for y_* and the uncertainty in the estimation, respectively.

The covariance function reflects the similarity between data points, i.e. the input points that are close have high covariance function, and

are likely to have similar response values (Zhao et al., 2016b). The four most common covariance functions, namely exponential, squared exponential, rational quadratic, and Matern 5/2 are used in this study. The exponential covariance function is defined as follows (Rasmussen and Williams, 2006):

$$k(x_i, x_j) = \sigma_f^2 exp(-\frac{r}{l}) \tag{9}$$

where σ_f is the standard deviation of the function, l is the characteristic length-scale which determines how rapidly the function varies with the input data (x), and r is the Euclidean distance between x_i and x_j, $r = \sqrt{(x_i - x_j)^T (x_i - x_j)}$. The squared exponential covariance function, defined by:

$$k(x_i, x_j) = \sigma_f^2 exp(-\frac{r^2}{2l^2}) \tag{10}$$

The rational quadratic one is defined as:

$$k(x_i, x_j) = \sigma_f^2 (1 + \frac{r^2}{2l^2\alpha^2})^{-\alpha} \tag{11}$$

where, α is a positive-valued scale-mixture parameter. And the Maten 5/2 covariance function is defined as follows:

$$k(x_i, x_j) = \sigma_f^2 (1 + \frac{\sqrt{5}r}{l} + \frac{5r^2}{3l^2}) exp(-\frac{\sqrt{5}r}{l}) \tag{12}$$

The parameters to be calibrated are σ_n^2, σ_f^2 and l when the exponential, squared exponential or Matern 5/2 is used as the covariance function. The parameter α is determined as well if the covariance function of rational quadratic is used. To achieve accurate model parameters, it is necessary to have a well-distributed training data. As the training data here is the location of the stations and the interferometric phase at the stations, the data should be well-distributed over the area of interest and have the phase values with high variance. In this way, the Euclidean distance (r in the covariance functions formula) between the training data and the testing data will not be large. As a result, the covariance function ($k(x_i,x_j)$) will increase, which in turn leads to a better prediction.

In order to estimate the differential STD map for the interferograms with large temporal baselines (> 12 days in this study), we use two connected small temporal baseline interferograms, and add their differential STD maps. As interferograms with large temporal baseline are a linear combination of the small temporal baselines ones, we can infer that if the correction is good enough on the small ones, it will be good on the large ones as well. The approach can be validated by comparing the differential STD values at the GNSS stations with their corresponding values in the estimated STD map.

2.5. Displacement retrieval

As mentioned before, the main challenge in large-scale InSAR processing is tropospheric corrections. Having estimated this using ML-approach presented in Section 2.4, the tropospherically corrected interferograms can be processed to retrieve the displacement field using the SBAS approach (Berardino et al., 2002). For the SBAS analysis, we select pixels with coherence greater than 0.4 in at least half of the stack of interferograms. It should be mentioned that as Norway is close to the polar region, ionospheric effect may affect the quality of C-band InSAR interferograms (Fattahi et al., 2017; Gomba et al., 2017; Jacobsen and Andalsvik, 2016; Liang et al., 2019). However, as the focus of the study is tropospheric correction, the contribution from the ionospheric errors are accounted for here by finding the best-fitting plane to the selected pixels in each interferogram, which is assumed to remove residual tropospheric errors as well. We then estimate and remove DEM errors based on the relationship between interferometric phase and perpendicular baseline. Finally, the displacement time-series is derived by least-squares inversion at each pixel.

3. Results

Figs. 5 and 6 show the performance of the machine learning-based technique (GP regression) developed in this study for correcting tropospheric artifacts of interferograms. To correct each interferogram, we

subtract from the original interferometric observations the estimated differential STD map and the fitted plane. Among 200 GNSS stations, roughly 73 stations fall within the processed region. Their location are shown on the original interferograms (a). We used the unwrapped phases of the original interferograms at the GNSS locations together with the GNSS locations as a training set (b) and the differential STD values as the response (c). Using the GP technique, we fit the models, shown in (d), and predict the differential STD values for the whole interferogram using the model (e). Finally, we apply the DEM error corrections, and the predicted differential STD on the original interferogram, and deramp the result (f).

We assess the performance of our method by computing the reduction in interferogram RMSE after correcting for the tropospheric phase as measures of the method quality. The result shows that using our method, the RMSE values reduce from 27 mm in "20160927–20161009" interferogram and 23 mm in "20161009–20161021" interferogram to 2 and 3 mm, respectively (reduction by 91.7% and 85.8%).

Using two differential STD maps for the short intervals (12 days), interferograms "20160927–20161009" and "20161009–20161027", we can now estimate the differential STD map for the interferogram "20160927–20161027" with longer interval (24 days). Fig. 7 shows the original interferogram, the differential STD resulted by the technique, and the corrected interferogram. As illustrated in Fig. 7 the result is very encouraging as it leads to the RMSE reduction of the original interferogram by 81%.

We validated the technique for the interferograms with longer intervals (like Fig. 7b), for which we have estimated the differential STD map using the maps derived by the interferograms with short temporal baseline (like Figs. 5e and 6e). To this end, we extracted the estimated differential STD values at the GNSS stations and compared them with their corresponding values derived from each GNSS station. As an example, Fig. 8 illustrates the scatter-plot of the estimated differential STD using the machine learning-based technique at the GNSS locations versus the differential STD derived from each GNSS stations for the interferogram "20160927–20161021". The RMSE of 2 cm, and the correlation of 96% between the estimations and observations indicates the efficiency of our approach. For the rest of the interferograms with large-temporal baselines the RMSE ranges from 1.35 to 5.3 cm, and the correlation from 0.94% to 0.99%.

4. Discussions

In this section, we compare the results of our method with those obtained by using ERA-Interim. We also quantify the performance of our results in terms of RMSE reduction in the short-interval SB interferograms, sensitivity of the ML approach to the training set size and their spatial distribution, the quality of the correction as a function of distance, and reliability of the displacement time-series derived by different correction methods. At the end of this section we also investigate whether our method removes the other phase components like the deformation and the ionospheric effects.

4.1. Assessment of the techniques performance

Fig. 9 shows exemplary performance of the ERA-Interim on two interferograms with short temporal baselines. Comparing the original interferogram (a and d) with the STD maps derived using ERA-Interim (b and e) exhibits a good correlation in their overall pattern. Following the DEM error and the deramping steps (explained in Section 2.5) on the tropospherically corrected interferograms (c and f), the results show that using ERA-Interim reduces the RMSE of the original interferograms from 2.7 cm in "20160927–20161009" interferogram and 2.3 cm in "20161009–20161021" interferogram to 2 and 1 cm, respectively. This leads to 23% and 57% reduction in RMSE using ERA-Interim. However, as it was presented in Section 3, our approach works much better on the
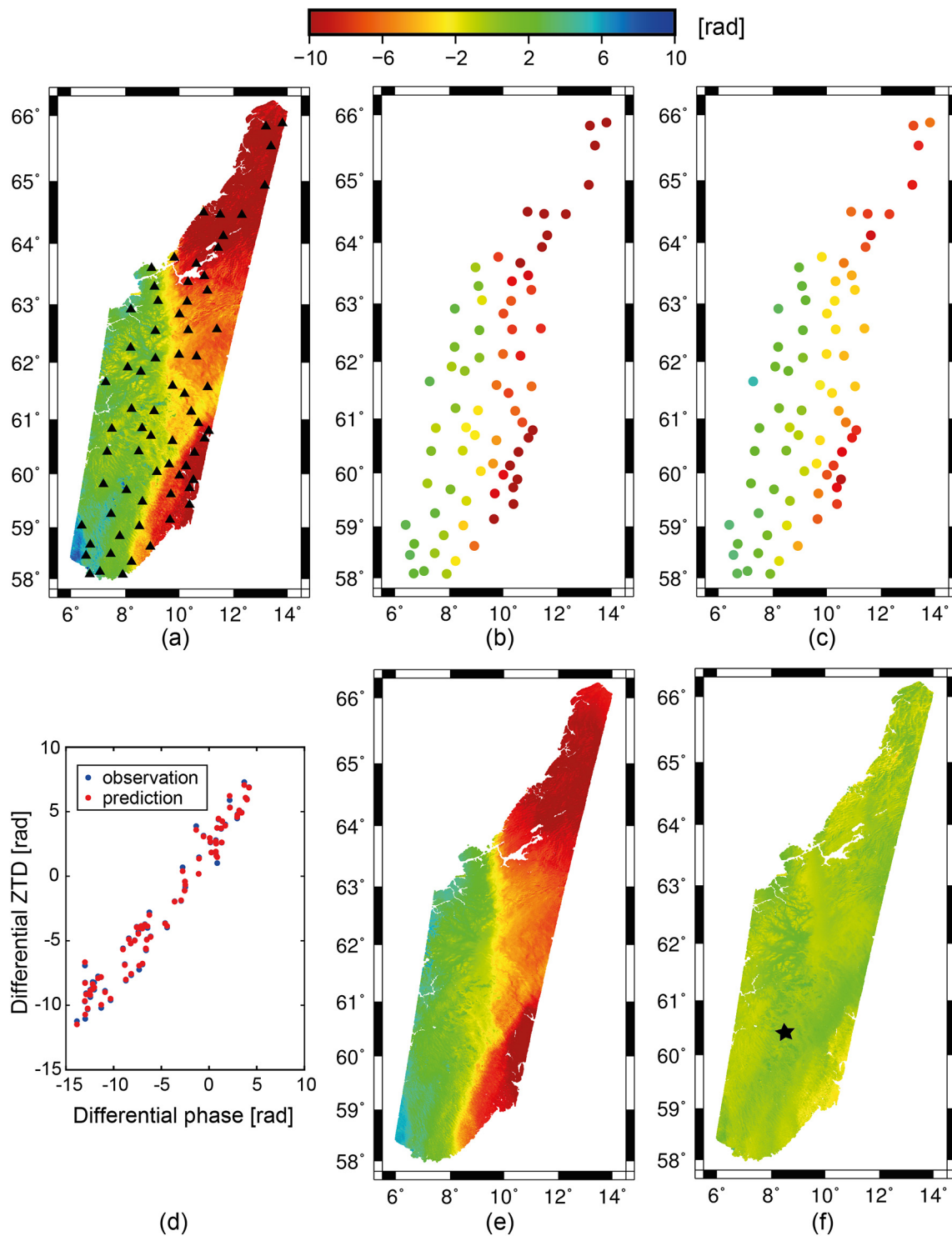
Fig. 6. An example of tropospheric corrections from InSAR and GNSS-based method (using machine learning) on the interferogram "20161009–20161021". (a) shows the original interferogram, (b–c) the unwrapped phases of the original interferograms and the differential STD values at the GNSS locations, respectively. (d) shows the training of the model, (e) the predicted differential STD, and (f) the corrected interferogram. The triangles in (a) show the location of the GNSS stations. The star in (f) shows the location of the reference area, which is one of the GNSS stations, and set for the all interferograms and STD maps.

same interferograms, reducing their RMSE to 2 and 3 mm.

We extend the above comparison and calculate RMSE for all interferograms with short-temporal baselines corrected with ERA-Interim and our proposed method (Table 1). As seen in Table 1 by using our approach, RMSE values of the original interferograms decreased by 70–92 %, while using the ERA-Interim they decreased by 20–75 %. On average ML-based approach leads to reduction of 83%, while ERA-Interim reduces the RMSE by 50%, clearly demonstrating the capability of our approach in mitigating tropospheric artifacts.

4.2. Sensitivity of the ML technique to training set size

During the ML-approach, for each interferogram with short-temporal baseline we first trained a model accurately using all available
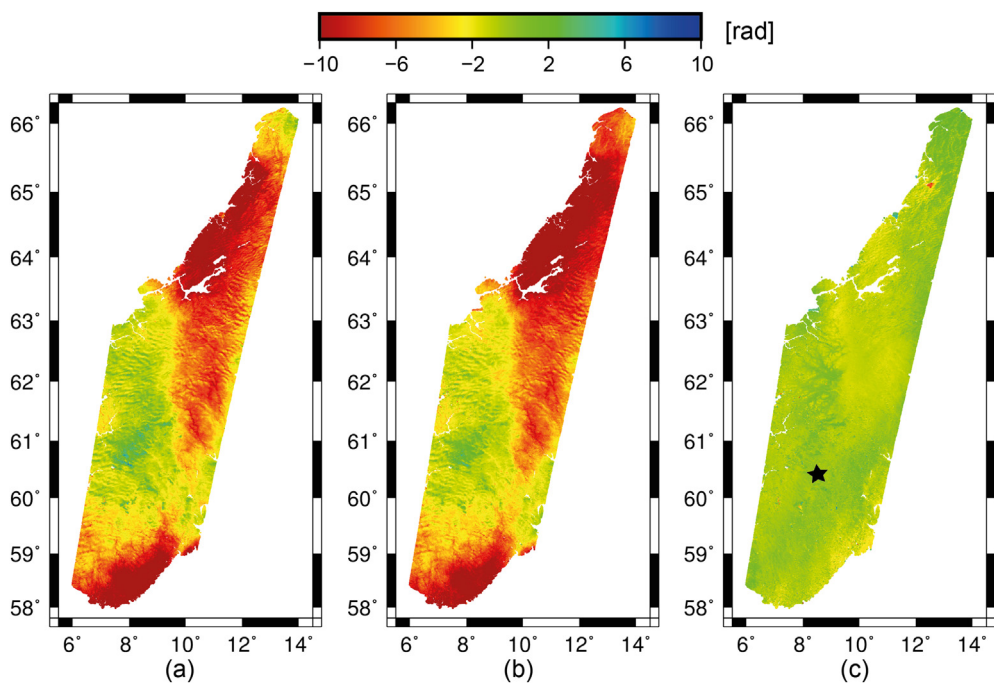
Fig. 7. An example of tropospheric corrections from InSAR and GNSS-based method (using machine learning) on the interferogram with longer interval (24 days) "20160927–20161021". (a) shows the original interferogram, (b) the estimated differential STD, and (c) the corrected interferogram. The star in (c) shows the location of the reference area, which is one of the GNSS stations, and set for the all interferograms and STD maps.
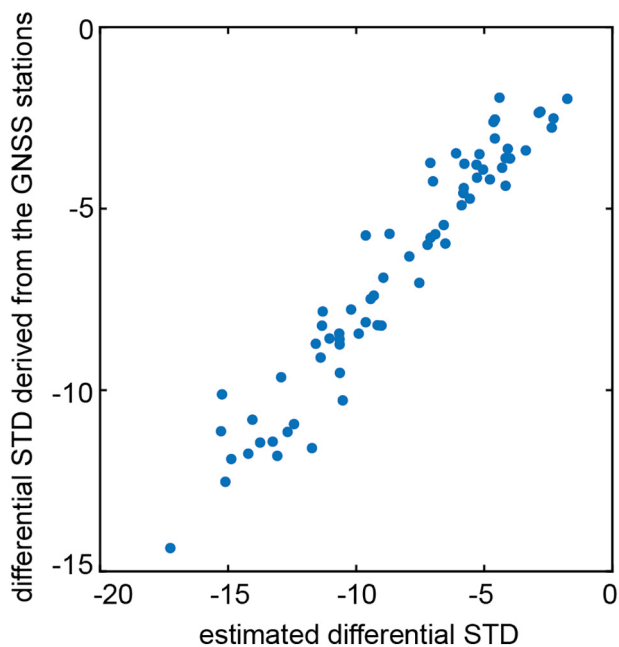

Fig. 8. Scatter-plot of the estimated differential STD using the machine learning-based technique at the GNSS locations versus the differential STD derived from each GNSS stations for the interferogram with longer interval (24 days), "20160927-20161021".

GNSS stations in the processed region (73 stations). To check if the approach is applicable for the regions with coarser GNSS network, we investigate the robustness of our approach to fewer GNSS stations to determine if it can be used to derive comparable modeling as obtained using all the stations. We achieved this by applying the test on the interferogram "20160927–20161009" and calculating the RMSE of the corrected interferogram using different number of the training data. The training accuracy is evaluated by computing the RMSE reduction of the corrected interferogram compared to the original one. Fig. 10 illustrates the changes of RMSE versus training set size by our method.

From Fig. 10, it is obvious that the reduction in RMSE of the

corrected interferogram compared to the original one using only 30% of the entire training data is approximately the same as that obtained by using the entire training set. For example, the RMSE reduces by ~80% using only 10% of training data (7 GNSS stations). This indicates that our approach is tolerant to training set size, having a good generalization capability even with a small set of training samples. The figure also shows that the accuracy decreases, when the training data size is reduced from 20% to 10% of the training set. This is caused by random selection of the training set, which is investigated in the next section.

4.3. Sensitivity of the ML technique to the spatial distribution of training data

As seen in Fig. 10, using 10% of the stations leads to a better correction than with 20% of the stations (~77% compared to ~82%). Better performance of the model with fewer stations suggests a certain sensitivity of the approach to the spatial distribution of the GNSS stations. We analyze this assumption using only 7 stations (10% of the training data) with different spatial distribution, all of which are located on the up, down, right, or left side of the processed region. We then apply the test on the interferogram "20160927–20161009". The analysis shows that the RMSE of the corrected interferogram reduces by around 56–80 % when the stations are on one side of the image (up, down, right, or left side of the processed region). However, in our experience the best result is achieved when the stations are distributed spatially-homogeneous over the whole processed region (RMSE reduction of 90%). This indicates that as samples become dispersed across the region of interest, training accuracy improves significantly. This is not surprising as a wider range of sampling in ML problems leads to have good representative samples of the data, which in turn results in better generalization capabilities (Cracknell and Reading, 2014; Harvey and Fotopoulos, 2016). As it is mentioned in Section 2.4, when the training data are located on one side of the image, the Euclidean distance between the training data and the testing data will be increased, which in turn reduces the covariance function and leads to have an unreliable prediction. Conversely, if they are distributed evenly across the interferogram, but their number is not large enough to properly represent the variability of the phase in interferograms with high variances, this will not lead to reliable prediction either.
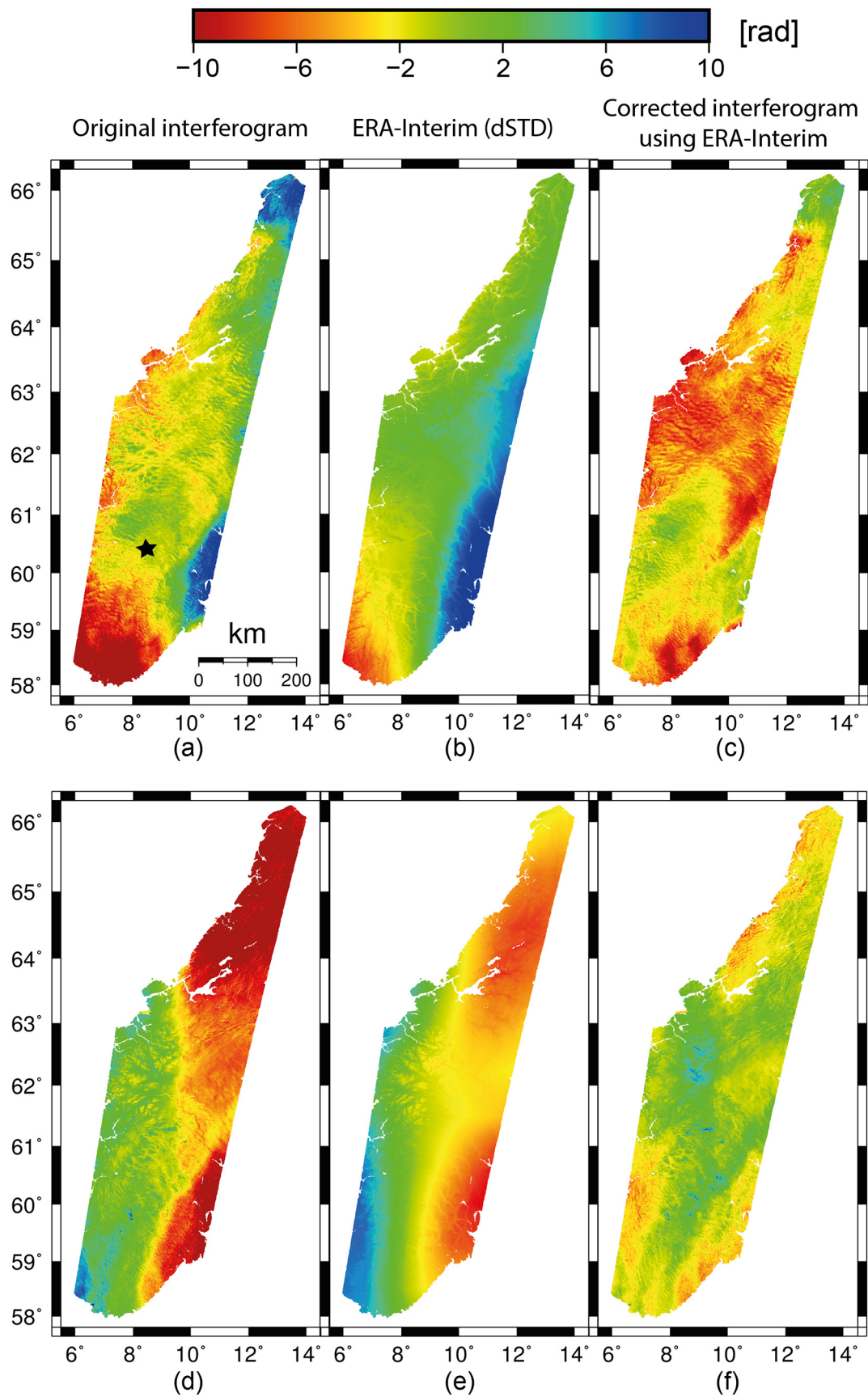
Fig. 9. Examples of tropospheric corrections from ERA-Interim. (a) shows the original interferogram ("20160927–20161009"), (b) the STD maps derived using ERA-Interim, and (c) shows the original interferogram after DEM error and the deramping and the tropospheric corrections. (d–f) similar to (a–c) but for interferogram "20161009–20161021". The star in (a) shows the location of the reference area, which is set for the all interferograms and STD maps.

Table 1

RMSE of the short-interval (12 days) interferograms without and with the tropospheric correction techniques. The unit is centimeter.

| Date [yyyymmdd] master_slave	Tropospheric correction technique		
	no-correction	ERA-Interim	ML
20160530_20160611	2.61	1.39	0.51
20160705_20160717	2.09	0.83	0.37
20160717_20160729	1.92	1.01	0.47
20160729_20160810	2.65	1.35	0.27
20160810_20160822	1.91	1.1	0.44
20160822_20160903	1.77	1.42	0.54
20160903_20160915	7.85	2	1.02
20160915_20160927	8.54	2.14	1.05
20160927_20161009	2.67	2.06	0.22
20161009_20161021	2.37	1.01	0.34
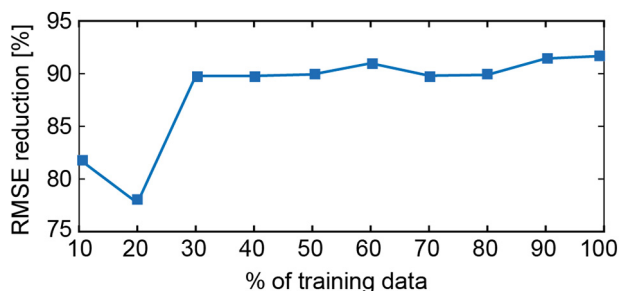
Fig. 10. Comparison of the RMSE reduction for the whole training set and fewer training data.

4.4. The quality of the correction as a function of distance

The uncertainty of the tropospheric correction is a function of distance (Emardson et al., 2003; Fattahi and Amelung, 2015). To investigate the quality of the correction as a function of distance to the GNSS stations, we used half of the stations for the model training and another half for the validation. We selected stations with different spatial distribution to increase the variability of the distance; all stations located in the up, bottom, middle part of the processed region or randomly distributed over the region. We compute the residual of the tropospheric delay (the predicated delay-known delay) for the stations that were not used in the training. Fig. 11a shows the residual of the delay for the stations, which were used as a test data versus the distance to the closest station, which were used as a training data. The figure shows that, as expected, the prediction error of the model increases by increasing the distance. To simplify the interpretation, we plotted in Fig. 11b the averaged residuals of the test stations within the bins with the width of 50 km distance from the training stations with their associated standard deviations.

4.5. Validation of the displacement time-series

To validate the tropospheric correction methods, we compare the InSAR derived time-series before and after corrections with those observed at each GNSS stations (Fig. 12). To this end, we projected the displacement in east, west, and up directions into the Sentinel-1 LOS direction with the formulation in (Hanssen, 2001). InSAR time-series are relative to a reference date, which is 20160729 (master image). GNSS time-series are referenced to the same reference date as InSAR time-series. All InSAR and GNSS time-series are referenced in space to the same area, which is one of the GNSS stations (the location is depicted in Fig. 9a with a star). Looking at the time-series plots, shows that the scatter of InSAR time-series significantly reduces after tropospheric delay correction. They can introduce errors of over 15 cm to ground surface displacement.

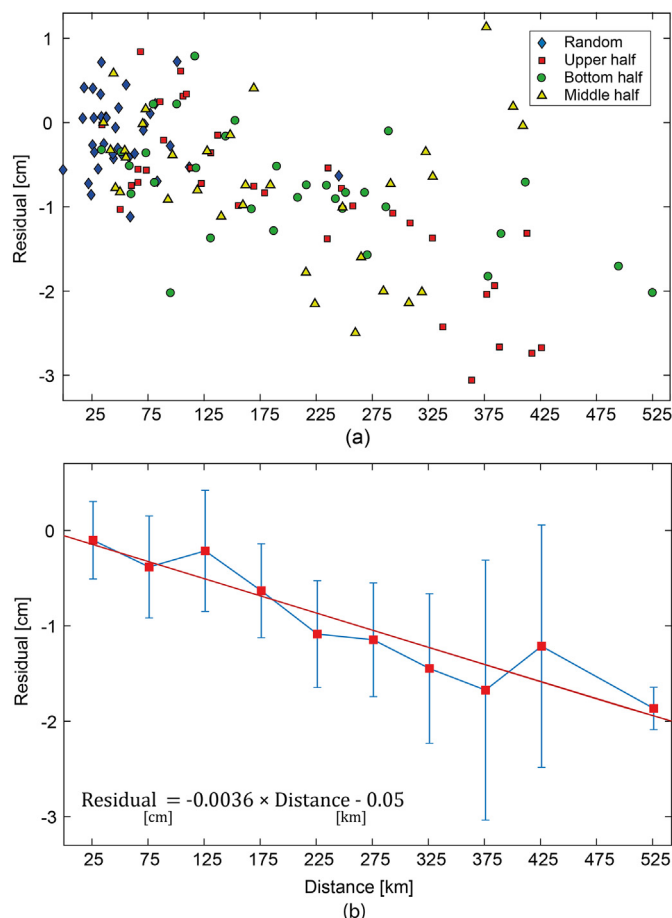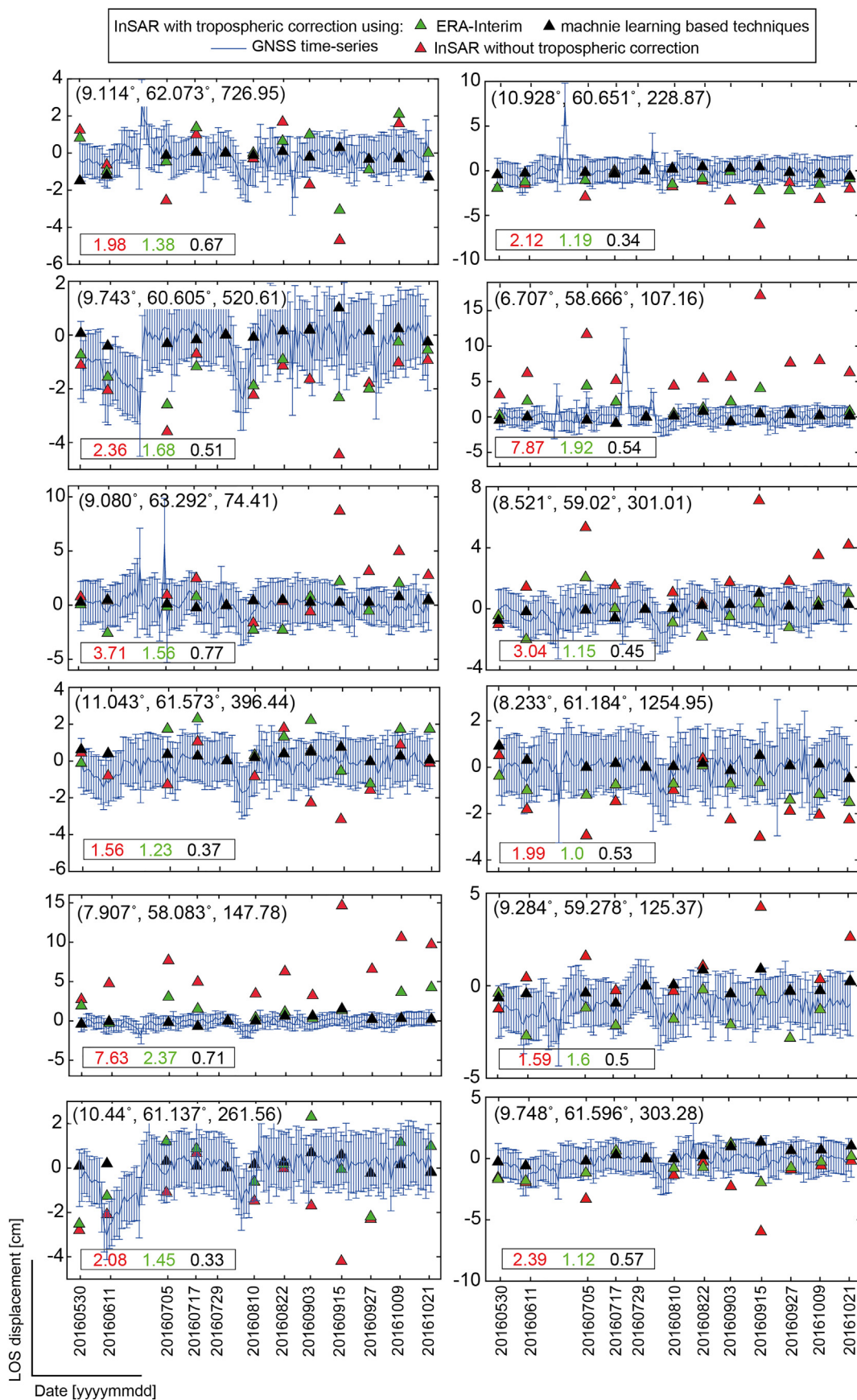To quantify the performance of the tropospheric correction, we

Fig. 11. (a) The residual of the tropospheric delay for the stations which used as a test data versus the distance to the closest station which used as a training data. The different sets of the training data are used with different spatial distribution; the stations located in the up, bottom, middle part of the processed region or randomly distributed over the processed region. (b) The averaged residuals of the test stations within the bins with the width of 50 km distance from the training stations. The bars show the associated standard deviations for each averaged residual. The equation on the left bottom corner shows the linear fitting to the graph, depicted by red line. (For interpretation of the references to color in this figure legend, the reader is referred to the web version of this article.)

compute the RMSE of InSAR time-series (before and after correction) relative to GNSS time-series measurements. As illustrated in Fig. 12, correction of tropospheric delay significantly improves the quality of the results, reducing the RMSE from 1.6 and 7.9 cm at different stations before correction to 1 and 2.4 cm after correction using ERA-Interim model. Compared to ERA-Interim, our proposed method works significantly better as it leads to the RMSE reduction of 3 to 7 mm. This indicates the importance of the tropospheric correction and in particular the effectiveness of our approach to deal with this problem.

4.6. Does the method remove the other phase components?

Here, we investigate whether our method simply mimics the interferogram and in turn removes other phase components, like ionospheric effects or ground deformation. Fig. 13 shows one of the unwrapped interferograms, "20160822–20160903", and the differential STD map derived using our method. Looking at the dSTD values at the GNSS stations on the tropospheric map (the circles in the Fig. 13b, which are used as training data), shows the good performance of the modeling. Comparing (Fig. 13a and b) shows that the response of the model is affected by the dSTD values at the GNSS stations and not by the

(caption on next page)

interferometric phase values at the stations. The modeling uses the interferometric phase values mainly for deriving the gradients of the dZTD changes in space. This shows that our method does not map all the interferometric phase onto the tropospheric delays.

As it can be seen in the figure, there is a clear difference between the interferogram and the tropospheric map in the northern part. As there is no (or very little) deformation in the interferograms, the difference might be because of ionospheric effects or inaccuracies in the tropospheric delay estimation at the stations.

Looking at the rate of the total electron content (TEC) index changes in these Sentinel-1 acquisition dates (Fig. 13c and d), shows that there was a high activity in the date 2016-09-03, especially in northern Norway. Therefore the high activity of the ionosphere can be

considered as the main explanation for such a difference.

As the modeling uses the ZTD estimation at the GNSS stations as response, the performance of the method is affected by the uncertainty in the ZTDs estimation as well. This uncertainty is introduced by a variety of factors including mapping functions, phase ambiguity, receiver clock corrections, satellite orbits, ionospheric delay, signal multi-path, and antenna related errors (Ning et al., 2016). For the analyzed interferogram ("20160822–20160903"), the standard deviations of the ZTD values at the stations range from around 5 to 10 mm, which is equal to 1 to 2.2 radians. Therefore, part of the differences seen in Fig. 13a–b is caused by the uncertainty in the ZTD estimation.

It is worth noting that as the training dataset for the modeling is not affected by deformation, the model does not learn anthing about
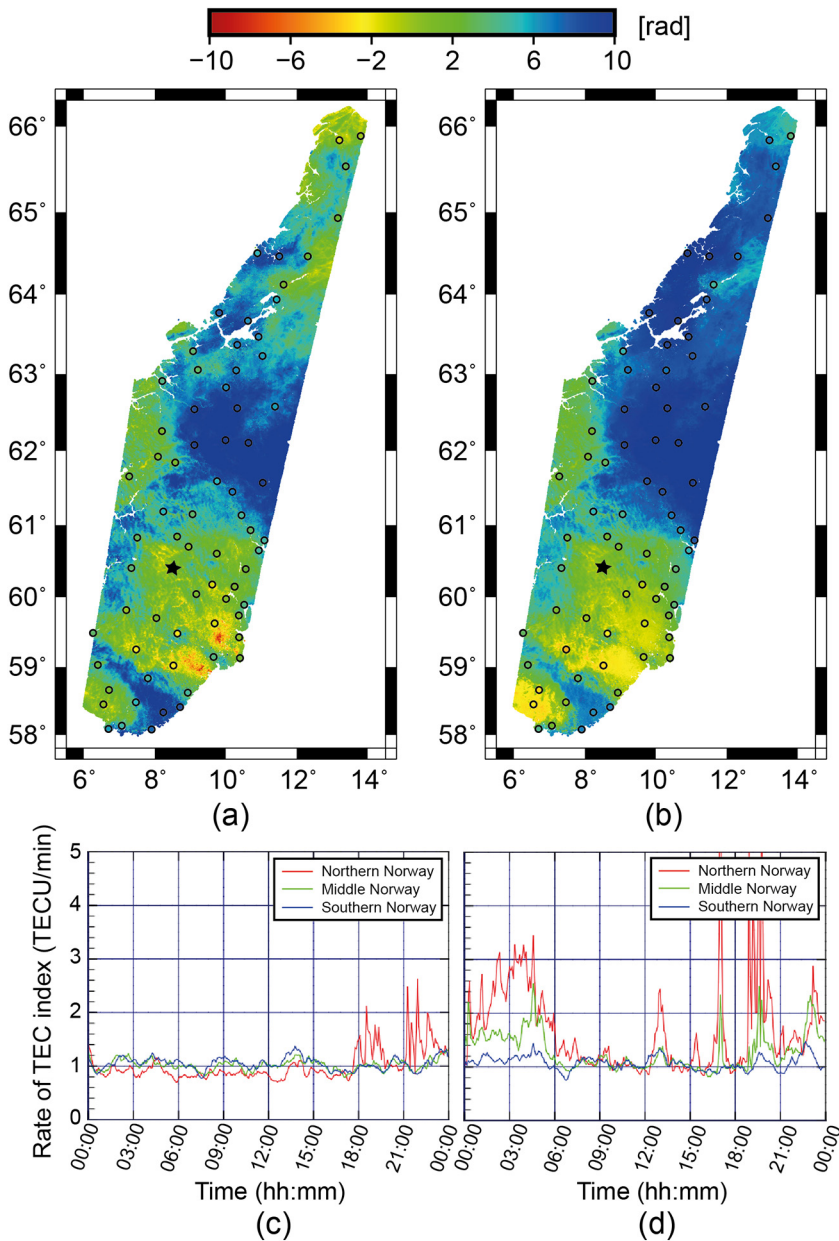

Fig. 13. An example of tropospheric map from InSAR and GNSS-based method (using machine learning) on the interferogram "20160822–20160903". (a) the original interferogram, and (b) the predicted differential STD map. (c and d) the mean rate of TEC index observed at ground location for northern, middle and southern Norway in the dates 20160822 and 20160903, respectively (Courtesy http://sesolstorm. kartverket.no). 0–1 TECU/min means the low activity, while 3–5 TECU/min means the high activity. The circles in (a and b) show the GNSS stations locations, color-coded by the interferometric phase and the differential STD values, respectively, used for the model training. The star in (a and b) shows the location of the reference area, which is one of the GNSS stations.

deformation signal. As a result the model can differentiate between tropospheric delay and deformation signal and perform well for areas other than Norway with higher deformation rates and/or in areas where deformation has correlation with topography. However, this needs to be investigated in more detail in future research.

5. Conclusions

Our study with Sentinel-1 data showed that ERA-Interim is not able to well reduce tropospheric phase delay in large-scale interferometric synthetic aperture radar (InSAR) measurements over Norway. We showed that our new technique based upon machine learning (ML) exploiting interferograms with short temporal baselines and global navigation satellite system (GNSS) derived zenith total delay (ZTD), improves tropospheric corrections on Sentinel-1 interferograms on average by 83% compared to 50% root-mean-square error (RMSE) reduction gained by using ERA-Interim. The technique facilitates the corrections, as we do not need to deal with finding a suitable function to interpolate the coarse model-node spacing. It is also robust in the case of few GNSS stations. However, the quality of the correction depends on the spatial distribution of the stations and is a function of distance to the stations. Comparing the displacement time-series based on small baseline subset (SBAS) on the interferograms corrected by our approach with GNSS measurements showed a good agreement, with overall RMSE of 5.2 mm compared to 14.7 mm derived by using the SBAS approach and the correction based on ERA-Interim.

CRediT authorship contribution statement

Roghayeh Shamshiri: Conceptualization, Methodology, Software, Formal analysis, Writing - original draft, Visualization. **Mahdi Motagh:** Conceptualization, Methodology, Writing - review & editing, Supervision. **Hossein Nahavandchi:** Conceptualization, Supervision, Funding acquisition. **Mahmud Haghshenas Haghighi:** Software, Formal analysis. **Mostafa Hoseini:** Software, Formal analysis.

Declaration of competing interest

The authors declare that they have no known competing financial interests or personal relationships that could have appeared to influence the work reported in this paper.

Acknowledgments

References

Bekaert, D., Walters, R., Wright, T., Hooper, A., Parker, D., 2015. Statistical comparison of insar tropospheric correction techniques. Remote Sens. Environ. 170, 40–47.

Bélisle, E., Huang, Z., Le Digabel, S., Gheribi, A.E., 2015. Evaluation of machine learning interpolation techniques for prediction of physical properties. Comput. Mater. Sci. 98, 170–177.

Bellinger, C., Jabbar, M.S.M., Zaïane, O., Osornio-Vargas, A., 2017. A systematic review of data mining and machine learning for air pollution epidemiology. BMC public

health 17, 907.

Berardino, P., Fornaro, G., Lanari, R., Sansosti, E., 2002. A new algorithm for surface deformation monitoring based on small baseline differential sar interferograms. IEEE Trans. Geosci. Remote Sens. 40, 2375–2383.

Berrisford, P., Dee, D., Poli, P., Brugge, R., Fielding, M., Fuentes, M., Kållberg, P., Kobayashi, S., Uppala, S., Simmons, A., 2011. 11/2011. The Era-Interim Archive Version 2.0. pp. 23.

Blaha, M., Vogel, C., Richard, A., Wegner, J.D., Pock, T., Schindler, K., 2016. Large-scale semantic 3d reconstruction: an adaptive multi-resolution model for multi-class volumetric labeling. In: Proceedings of the IEEE Conference on Computer Vision and Pattern Recognition, pp. 3176–3184.

Cetin, E., Cakir, Z., Meghraoui, M., Ergintav, S., Akoglu, A.M., 2014. Extent and distribution of aseismic slip on the ismetpaşa segment of the north Anatolian Fault (Turkey) from persistent scatterer insar. Geochem. Geophys. Geosyst. 15, 2883–2894.

Chen, S., Wang, H., Xu, F., Jin, Y.-Q., 2016. Target classification using the deep convolutional networks for SAR images. IEEE Trans. Geosci. Remote Sens. 54, 4806–4817.

Chen, Y., Zhao, X., Jia, X., 2015. Spectral-spatial classification of hyperspectral data based on deep belief network. IEEE J. Sel. Topics Appl. Earth Obs. Remote Sens. 8, 2381–2392.

Cortes, C., Vapnik, V., 1995. Support-vector networks. Mach. Learn. 20, 273–297.

Cracknell, M.J., Reading, A.M., 2014. Geological mapping using remote sensing data: a comparison of five machine learning algorithms, their response to variations in the spatial distribution of training data and the use of explicit spatial information. Comput. Geol. 63, 22–33.

Daout, S., Doin, M.-P., Peltzer, G., Socquet, A., Lasserre, C., 2017. Large-scale insar monitoring of permafrost freeze-thaw cycles on the Tibetan Plateau. Geophys. Res. Lett. 44, 901–909.

Delacourt, C., Briole, P., Achache, J., 1998. Tropospheric corrections of SAR interferograms with strong topography. Application to Etna. Geophys. Res. Lett. 25, 2849–2852.

Dietterich, T., 1995. Overfitting and undercomputing in machine learning. ACM Comput. Surv. 27, 326–327.

Do, C.B., 2007. Gaussian Processes. accessed Dec 5. Stanford University, Stanford, CA, pp. 2017.

Doin, M.P., Lasserre, C., Peltzer, G., Cavalié, O., Doubre, C., 2009. Corrections of stratified tropospheric delays in SAR interferometry: validation with global atmospheric models. J. Appl. Geophys. 69, 35–50.

Domingos, P.M., 2012. A few useful things to know about machine learning. Commun. acm 55, 78–87.

Duan, Y., Liu, F., Jiao, L., Zhao, P., Zhang, L., 2017. SAR image segmentation based on convolutional-wavelet neural network and Markov random field. Pattern Recogn. 64, 255–267.

Emadali, L., Motagh, M., Haghshenas Haghighi, M., 2017. Characterizing post-construction settlement of the masjed-soleyman embankment dam, southwest Iran, using terrasar-x spotlight radar imagery. Eng. Struct. 143, 261–273.

Emardson, T., Simons, M., Webb, F., 2003. Neutral atmospheric delay in interferometric synthetic aperture radar applications: statistical description and mitigation. J. Geophys. Res. Solid Earth 108.

Fattahi, H., Agram, P., Simons, M., 2016. A network-based enhanced spectral diversity approach for tops time-series analysis. IEEE Trans. Geosci. Remote Sens. 55, 777–786.

Fattahi, H., Amelung, F., 2015. Insar bias and uncertainty due to the systematic and stochastic tropospheric delay. J. Geophys. Res. Solid Earth 120, 8758–8773.

Fattahi, H., Simons, M., Agram, P., 2017. Insar time-series estimation of the ionospheric phase delay: an extension of the split range-spectrum technique. IEEE Trans. Geosci. Remote Sens. 55, 5984–5996.

Feng, W., Lindsey, E., Barbot, S., Samsonov, S., Dai, K., Li, P., Li, Z., Almeida, R., Chen, J., Xu, X., 2017. Source characteristics of the 2015 MW 7.8 Gorkha (Nepal) earthquake and its MW 7.2 aftershock from space geodesy. Tectonophysics 712, 747–758.

Ferretti, A., Colombo, D., Fumagalli, A., Novali, F., Rucci, A., 2015. Insar data for monitoring land subsidence: time to think big. Proc. Int. Assoc. Hydrol. Sci. 372, 331–334.

Ferretti, A., Fumagalli, A., Novali, F., Prati, C., Rocca, F., Rucci, A., 2011. A new algorithm for processing interferometric data-stacks: Squeesar. IEEE Trans. Geosci. Remote Sens. 49, 3460–3470.

Ferretti, A., Prati, C., Rocca, F., 2001. Permanent scatterers in SAR interferometry. IEEE Trans. Geosci. Remote Sens. 39, 8–20.

Fielding, E.J., Sangha, S.S., Bekaert, D.P., Samsonov, S.V., Chang, J.C., 2017. Surface deformation of north-central Oklahoma related to the 2016 MW 5.8 Pawnee earthquake from SAR interferometry time series. Seismol. Res. Lett. 88, 971–982.

Gomba, G., González, F.R., De Zan, F., 2017. Ionospheric phase screen compensation for the sentinel-1 tops and alos-2 scansar modes. IEEE Trans. Geosci. Remote Sens. 55, 223–235.

Haghshenas Haghighi, M., Motagh, M., 2016. Assessment of ground surface displacement in Taihape landslide, New Zealand, with c-and x-band SAR interferometry. N. Z. J. Geol. Geophys. 59, 136–146.

Haghshenas Haghighi, M., Motagh, M., 2017. Sentinel-1 insar Over Germany: Large-scale Interferometry, Atmospheric Effects, and Ground Deformation Mapping.

Haghshenas Haghighi, M., Motagh, M., 2018. Mining big data of sentinel-1 to detect and monitor land subsidence in wide scale: Example from sinking aquifers in iran. In: AGU Fall Meeting.

Haghshenas Haghighi, M., Motagh, M., 2019. Ground surface response to continuous compaction of aquifer system in Tehran, Iran: results from a long-term multi-sensor insar analysis. Remote Sens. Environ. 221, 534–550.

Hane, C., Zach, C., Cohen, A., Angst, R., Pollefeys, M., 2013. Joint 3d scene reconstruction and class segmentation. In: Proceedings of the IEEE Conference on Computer Vision

and Pattern Recognition, pp. 97–104.

Hanssen, R.F., 2001. Radar Interferometry: Data Interpretation and Error Analysis. 2 Springer Science & Business Media.

Harvey, A., Fotopoulos, G., 2016. Geological mapping using machine learning algorithms. Int. Arch. Photogramm. Remote. Sens. Spat. Inf. Sci. 41.

Herring, T., King, R., Floyd, M., McClusky, S., 2018. Introduction to gamit/globk. Massachusetts Institute of Technology, Cambridge, Massachusetts.

Hooper, A., Zebker, H., Segall, P., Kampes, B., 2004. A new method for measuring deformation on volcanoes and other natural terrains using insar persistent scatterers. Geophys. Res. Lett. 31.

Hu, F., Xia, G.-S., Hu, J., Zhang, L., 2015. Transferring deep convolutional neural networks for the scene classification of high-resolution remote sensing imagery. Remote Sens. 7, 14680–14707.

Hu, Y., Yao, Y., 2018. A new method for vertical stratification of zenith tropospheric delay. Adv. Space Res.

Hu, Z., Mallorquí, J.J., 2019. An accurate method to correct atmospheric phase delay for insar with the era5 global atmospheric model. Remote Sens. 11, 1969.

Huang, G.-B., Zhou, H., Ding, X., Zhang, R., 2012. Extreme learning machine for regression and multiclass classification. IEEE Trans. Syst. Man Cybern. B Cybern. 42, 513–529.

Huang, W., Xiao, L., Wei, Z., Liu, H., Tang, S., 2015. A new pan-sharpening method with deep neural networks. IEEE Geosci. Remote Sens. Lett. 12, 1037–1041.

Hussain, E., Wright, T.J., Walters, R.J., Bekaert, D.P., Lloyd, R., Hooper, A., 2018. Constant strain accumulation rate between major earthquakes on the north Anatolian fault. Nat. Commun. 9, 1392.

Intrieri, E., Raspini, F., Fumagalli, A., Lu, P., Del Conte, S., Farina, P., Allievi, J., Ferretti, A., Casagli, N., 2018. The maoxian landslide as seen from space: detecting precursors of failure with sentinel-1 data. Landslides 15, 123–133.

Jacobsen, K.S., Andalsvik, Y.L., 2016. Overview of the 2015 St. Patricks Day storm and its consequences for rtk and ppp positioning in Norway. J. Space Weather and Space Climate 6, A9.

Jacobsen, K.S., Schäfer, S., 2012. Observed effects of a geomagnetic storm on an rtk positioning network at high latitudes. J. Space Weather and Space Climate 2, A13.

Jo, M.J., Won, J.S., Kim, S.-W., Jung, H.S., 2010. A time-series SAR observation of surface deformation at the southern end of the San Andreas Fault zone. Geosciences J. 14, 277–287.

Jolivet, R., Grandin, R., Lasserre, C., Doin, M.-P., Peltzer, G., 2011. Systematic insar tropospheric phase delay corrections from global meteorological reanalysis data. Geophys. Res. Lett. 38.

Kalia, A., Frei, M., Lege, T., 2017. A Copernicus downstream-service for the nationwide monitoring of surface displacements in Germany. Remote Sens. Environ. 202, 234–249.

Kaneko, Y., Fialko, Y., Sandwell, D., Tong, X., Furuya, M., 2013. Interseismic deformation and creep along the central section of the north Anatolian Fault (Turkey): Insar observations and implications for rate-and-state friction properties. J. Geophys. Res. Solid Earth 118, 316–331.

Li, J., Heap, A.D., Potter, A., Daniell, J.J., 2011. Application of machine learning methods to spatial interpolation of environmental variables. Environ. Model Softw. 26, 1647–1659.

Li, Z., Fielding, E.J., Cross, P., Muller, J.-P., 2006. Interferometric synthetic aperture radar atmospheric correction: Gps topography-dependent turbulence model. J. Geophys. Res. Solid Earth 111.

Liang, C., Agram, P., Simons, M., Fielding, E.J., 2019. Ionospheric correction of insar time series analysis of c-band sentinel-1 tops data. IEEE Trans. Geosci. Remote Sens.

Liaw, A., Wiener, M., et al., 2002. Classification and regression by randomforest. R news 2, 18–22.

Lubitz, C., Motagh, M., Wetzel, H.-U., Kaufmann, H., 2013. Remarkable urban uplift in Staufen im Breisgau, Germany: observations from terrasar-x insar and leveling from 2008 to 2011. Remote Sens. 5, 3082–3100.

Milillo, P., Giardina, G., DeJong, M., Perissin, D., Milillo, G., 2018. Multi-temporal insar structural damage assessment: the London crossrail case study. Remote Sens. 10, 287.

Mirzaee, S., Motagh, M., Akbari, B., Wetzel, H., Roessner, S., 2017. Evaluating three insar time-series methods to assess creep motion, case study: Masouleh landslide in north Iran. ISPRS Ann. Photogram., Remote Sens. Spatial Inf. Sci. 4.

Morales Rivera, A.M., Amelung, F., Mothes, P., Hong, S.-H., Nocquet, J.-M., Jarrin, P., 2017. Ground deformation before the 2015 eruptions of Cotopaxi Volcano detected by insar. Geophys. Res. Lett. 44, 6607–6615.

Motagh, M., Schurr, B., Anderssohn, J., Cailleau, B., Walter, T.R., Wang, R., Villotte, J.-P., 2010. Subduction earthquake deformation associated with 14 November 2007, mw 7.8 tocopilla earthquake in Chile: results from insar and aftershocks. Tectonophysics 490, 60–68.

Motagh, M., Shamshiri, R., Haghshenas Haghighi, M., Wetzel, H.-U., Akbari, B., Nahavandchi, H., Roessner, S., Arabi, S., 2017. Quantifying groundwater exploitation induced subsidence in the Rafsanjan Plain, southeastern Iran, using insar time-series and in situ measurements. Eng. Geol. 218, 134–151.

Nannini, M., Prats-Iraola, P., De Zan, F., Geudtner, D., 2016. Tops time series performance assessment with terrasar-x data. IEEE J. Sel. Topics Appl. Earth Obs. Remote Sens. 9, 3832–3848.

Ning, T., Wang, J., Elgered, G., Dick, G., Wickert, J., Bradke, M., Sommer, M., Querel, R., Smale, D., 2016. The uncertainty of the atmospheric integrated water vapour estimated from GNSS observations. Atmos. Meas. Tech. 9, 79–92.

Onn, F., Zebker, H., 2006. Correction for interferometric synthetic aperture radar atmospheric phase artifacts using time series of zenith wet delay observations from a GPS network. J. Geophys. Res. Solid Earth 111.

Prats-Iraola, P., Scheiber, R., Marotti, L., Wollstadt, S., Reigber, A., 2012. Tops

interferometry with terrasar-x. IEEE Trans. Geosci. Remote Sens. 50, 3179–3188.

Rasmussen, C.E., 2004. Gaussian processes in machine learning. In: Advanced Lectures on Machine Learning. Springer, pp. 63–71.

Rasmussen, C.E., Williams, C.K., 2006. Gaussian processes for machine learning. 2006. In: 38. The MIT Press, Cambridge, MA, USA, pp. 715–719.

Raspini, F., Bianchini, S., Ciampalini, A., Del Soldato, M., Solari, L., Novali, F., Del Conte, S., Rucci, A., Ferretti, A., Casagli, N., 2018. Continuous, semi-automatic monitoring of ground deformation using sentinel-1 satellites. Sci. Rep. 8.

Raspini, F., Moretti, S., Casagli, N., 2013. Landslide mapping using squeesar data: Giampilieri (Italy) case study. In: Landslide science and practice. Springer, pp. 147–154.

Samsonov, S.V., Trishchenko, A.P., Tiampo, K., González, P.J., Zhang, Y., Fernández, J., 2014. Removal of systematic seasonal atmospheric signal from interferometric synthetic aperture radar ground deformation time series. Geophys. Res. Lett. 41, 6123–6130.

Santara, A., Mani, K., Hatwar, P., Singh, A., Garg, A., Padia, K., Mitra, P., 2017. Bass net: band-adaptive spectral-spatial feature learning neural network for hyperspectral image classification. IEEE Trans. Geosci. Remote Sens. 55, 5293–5301.

Sawaf, F., Groves, R.M., 2014. Phase discontinuity predictions using a machine-learning trained kernel. Appl. Opt. 53, 5439–5447.

Scheiber, R., Moreira, A., 2000. Coregistration of interferometric SAR images using spectral diversity. IEEE Trans. Geosci. Remote Sens. 38, 2179–2191.

Shamshiri, R., Motagh, M., Baes, M., Sharifi, M.A., 2014. Deformation analysis of the Lake Urmia causeway (luc) embankments in northwest Iran: insights from multi-sensor interferometric synthetic aperture radar (insar) data and finite element modeling (fem). J. Geodesy 88, 1171–1185.

Shamshiri, R., Nahavandchi, H., Motagh, M., Hooper, A., 2018. Efficient ground surface displacement monitoring using sentinel-1 data: integrating distributed scatterers (ds) identified using two-sample t-test with persistent scatterers (ps). Remote Sens. 10, 794.

Smith, E.K., Weintraub, S., 1953. The constants in the equation for atmospheric refractive index at radio frequencies. Proc. IRE 41, 1035–1037.

Solari, L., Raspini, F., Del Soldato, M., Bianchini, S., Ciampalini, A., Ferrigno, F., Tucci, S., Casagli, N., 2018. Satellite radar data for back-analyzing a landslide event: the Ponzano (Central Italy) case study. Landslides 15, 773–782.

Spaans, K., Hooper, A., 2016. Insar processing for volcano monitoring and other near-real time applications. J. Geophys. Res. Solid Earth 121, 2947–2960.

Spoorthi, G.E., Gorthi, S., Gorthi, R.K.S.S., 2019. Phasenet: a deep convolutional neural network for two-dimensional phase unwrapping. IEEE Signal Process Lett. 26, 54–58.

Tang, W., Yuan, P., Liao, M., Balz, T., 2018. Investigation of ground deformation in Taiyuan Basin, China from 2003 to 2010, with atmosphere-corrected time series insar. Remote Sens. 10, 1499.

Torres, R., Snoeij, P., Geudtner, D., Bibby, D., Davidson, M., Attema, E., Potin, P., Rommen, B., Floury, N., Brown, M., et al., 2012. Gmes sentinel-1 mission. Remote Sens. Environ. 120, 9–24.

Vajedian, S., Motagh, M., Nilfouroushan, F., 2015. Stamps improvement for deformation analysis in mountainous regions: implications for the Damavand Volcano and Mosha Fault in Alborz. Remote Sens. 7, 8323–8347.

Viola, P., Jones, M., 2001. Rapid object detection using a boosted cascade of simple features. In: Computer Vision and Pattern Recognition, 2001. CVPR 2001. Proceedings of the 2001 IEEE Computer Society Conference on IEEE.

Walter, T.R., Motagh, M., 2014. Deflation and inflation of a large magma body beneath Uturuncu Volcano, Bolivia? Insights from insar data, surface lineaments and stress modelling. Geophys. J. Int. 198, 462–473.

Wegmüller, U., Werner, C., 1997. Gamma SAR processor and interferometry software. ESA SP 1687–1692.

Wessel, P., Smith, W.H., Scharroo, R., Luis, J., Wobbe, F., 2013. Generic mapping tools: improved version released. Eos. Trans. AGU 94, 409–410.

Wilgan, K., Geiger, A., 2018. High-resolution models of tropospheric delays and refractivity based on gnss and numerical weather prediction data for alpine regions in Switzerland. J. Geodesy 1–17.

Williams, S., Bock, Y., Fang, P., 1998. Integrated satellite interferometry: tropospheric noise, GPS estimates and implications for interferometric synthetic aperture radar products. J. Geophys. Res. Solid Earth 103, 27051–27067.

Yu, C., Li, Z., Penna, N.T., 2018. Interferometric synthetic aperture radar atmospheric correction using a GPS-based iterative tropospheric decomposition model. Remote Sens. Environ. 204, 109–121.

Yu, C., Penna, N.T., Li, Z., 2017. Generation of real-time mode high-resolution water vapor fields from GPS observations. J. Geophys. Res.-Atmos. 122, 2008–2025.

Zebker, H.A., Rosen, P.A., Hensley, S., 1997. Atmospheric effects in interferometric synthetic aperture radar surface deformation and topographic maps. J. Geophys. Res. Solid Earth 102, 7547–7563.

Zhao, B., Zhong, Y., Xia, G.-S., Zhang, L., 2016a. Dirichlet-derived multiple topic scene classification model for high spatial resolution remote sensing imagery. IEEE Trans. Geosci. Remote Sens. 54, 2108–2123.

Zhao, Y., Yin, F., Gunnarsson, F., Hultkratz, F., Fagerlind, J., 2016b. Gaussian processes for flow modeling and prediction of positioned trajectories evaluated with sports data. In: 2016 19th international conference on information fusion (FUSION), pp. 1461–1468.

Zhong, J., Yang, B., Huang, G., Zhong, F., Chen, Z., 2016. Remote sensing image fusion with convolutional neural network. Sens. Imag. 17, 10.

Zhu, X.X., Tuia, D., Mou, L., Xia, G.-S., Zhang, L., Xu, F., Fraundorfer, F., 2017. Deep learning in remote sensing: a comprehensive review and list of resources. IEEE Geosci. Remote Sens. Mag. 5, 8–36.